PHYSICAL REVIEW E **109**, 055205 (2024)

Photoionization process of the hydrogenlike carbon ion embedded in warm and hot dense plasmas

S. M. Lu,[1,2] F. Y. Zhou,[2,*] L. Y. Xie,[4] Y. L. Ma,[4] G. P. Zhao,[6] X. Gao,[2] Y. Wu,[2,3,5,†] and J. G. Wang[2,3,1]
[1]*Institute of Modern Physics, Fudan University, Shanghai 200433, China*
[2]*National Key Laboratory of Computational Physics, Institute of Applied Physics and Computational Mathematics, Beijing 100088, China*
[3]*School of Physics and Information Technology, Shaanxi Normal University, Xi'an 710119, China*
[4]*Key Laboratory of Atomic and Molecular Physics and Functional Materials of Gansu Province and College of Physics and Electronic Engineering, Northwest Normal University, Lanzhou 730070, China*
[5]*Center for Applied Physics and Technology, College of Engineering, Peking University, Beijing 100871, China*
[6]*College of Data Science, Jiaxing University, Jiaxing 314001, China*

(Received 15 February 2024; accepted 30 April 2024; published 29 May 2024)

Complicated many-body interactions between ions and surrounding particles exist in warm and hot dense plasmas. It will significantly alter the atomic structures and dynamic properties of the embedded ions. Recently, the atomic-state-dependent (ASD) screening model has been proposed and shown to be valid for investigating the screening effect in warm and hot dense plasmas over a wide range of electron densities and temperatures. By employing the ASD model, we investigate the photoionization process for the hydrogenlike carbon ion embedded in warm and hot dense plasmas with corresponding Coulomb coupling parameter ranges of $0.05 \leqslant \Gamma \leqslant 1.16$, where Γ characterizes the ratio of the average potential to thermal energy. It is found that there are stronger plasma screening effects on the ionization energy and photoionization cross section due to the negative-energy electron distributions considered in the ASD model compared to those considering only free electrons. The present results from the ASD model show reasonable agreement with the classical Debye-Hückel (DH) model in weakly coupled plasmas. However, significant deviations of the ionization energy and cross section between these two models are observed in moderately and strongly coupled plasmas, due to the approximate treatment of the plasma-electron density distribution of the DH model. In the region of low photoelectron energies, the positions of the shape resonance peaks of the cross sections obtained from the ASD model differ significantly from those of the DH model due to the different screening effects.

DOI: 10.1103/PhysRevE.109.055205

I. INTRODUCTION

Warm and hot dense plasma exists widely in inertial confinement fusion (ICF) experiments, and in various astronomical objects such as stars and the interiors of giant planets [1–4]. It is crucial to determine the atomic parameters of the ions embedded in these plasmas for both fundamental research and practical applications. The photoionization cross section is a key parameter in the calculation of the radiation opacity, which plays an important role in the study of stellar structure and evolution [5,6]. It should be noted that one of the most significant features of the photoionization cross section using the Coulomb potential is shape resonance, which appears due to the centrifugal barrier in the effective potential of the continuum channel. The cross section of the non-Coulomb potential reflects more features, including shape resonance, Cooper minima, low-energy Wigner threshold law, and virtual state resonances [7–12]. Meanwhile, the plasma environment effect can decrease the binding energy from the nucleus, resulting in the redshift [13] for the photoionization threshold.

To investigate the plasma effect on the atomic structure and dynamic processes, a series of screening model potentials have been developed to describe the interaction between charged particles in plasmas [14–16]. For weakly coupled plasmas, Young-Dae Jung *et al.* have presented energy levels, photoionization cross sections, and resonance characteristics near the ionization threshold for alkali-metal atoms [17,18], hydrogen and helium atoms [19–21], and H-like and He-like ions [10,18,22] using different computational schemes with the Debye-Hückel screening potential [14,23]. They have found that the plasma screening effect significantly impacts the photoionization cross section, and also plays an important role in determining the cross-section characteristics, including phenomena like the Cooper minimum and shape resonance. In the case of strongly coupled plasmas, the ion sphere model (ISP) [15] has been proposed to account for particle interaction in dense plasmas. This model considers a condition at high plasma density and is temperature independent. Das *et al.* have reported the important influence of plasma screening on energy levels and photoionization cross sections for H-like [24,25], Li-like [24], and F-like [26] ions in strongly coupled plasmas. In addition, the cosine Debye-Hückel potential has been applied to describe quantum plasma at extremely low temperatures [27,28]. However, research on warm and hot dense plasma is limited due to the

---

[*] Corresponding author: zhou_fuyang@iapcm.ac.cn

[†] wu_yong@iapcm.ac.cn

complex multibody correlations involved in dense plasma models. Moreover, the prediction results have discrepancies with the spectra, line shifts, and ionization potential depressions in the latest high-precision spectroscopy experiment at warm and hot dense plasmas [29]. It is necessary to investigate the influence of plasma screening on the physical quantities related to the photoionization process, including wavefunctions, energy levels, and cross sections, using appropriate screening models. Recently, Zhou *et al.* [29] have proposed an atomic-state-dependent (ASD) screening model. Compared to the most popular DH and ISP models, the ASD model takes into account the negative-energy electron density distributions generated by inelastic collision processes containing three-body recombination, which becomes important in warm and hot dense plasmas [30]. The ASD screening model can describe the screening effect in moderately coupled plasmas, and converges to the DH and ISP models under the conditions of weakly coupled and strongly degenerate plasmas [29].

In this work, the photoionization process of the hydrogenlike carbon ion is investigated by employing an atomic-state-dependent screening model. We investigate the photoionization process of the hydrogenlike carbon ion, which is a significant component in ICF experiments and simulations [31,32]. In Sec. II, we present the screening model potential, along with the methodology used to solve the Dirac equation for the hydrogenlike ion and calculate the photoionization cross section. In Sec. III, we illustrate the results and discussions of the wavefunctions and ionization energies for the hydrogenlike carbon ion embedded in warm and hot dense plasmas, as well as the plasma effects on photoionization cross sections. In Sec. IV, we show our conclusions based on the findings.

Atomic units (a.u.) will be used in the remaining part of this paper unless explicitly indicated otherwise.

II. THEORETICAL METHOD

A. Atomic-state-dependent screening model potential

In weakly coupled plasmas, the well-known Debye-Hückel potential is applied to describe the electron-ion interaction formed as [14,23]

$$V(r) = -\frac{Z}{r}\exp(-r/\lambda_D), \tag{1}$$

with Debye screening length $\lambda_D = (T_e/4\pi n_e)^{1/2}$. In the DH model, the electron density distribution $\rho(r) = \rho_0[1 + \Phi(r)/T]$ is the first-order Taylor approximation of the Boltzmann distribution function $\rho(r) = \rho_0 \exp[-\Phi(r)/T]$ with the total effective potential $\Phi(r)$ at position r. It suggests that the DH model is valid only in weakly coupled plasmas ($\Gamma \ll 1$), while invalid in moderately coupled ($\Gamma \sim 1$) or strongly coupled ($\Gamma > 1$) plasmas, in which complex multibody correlation effects play a key role. The Coulomb coupling parameter Γ is described by the ratio of the potential energy of neighboring particles to the thermal energy, and can be denoted as $\Gamma = 1/\overline{a}T_e$ [14,33]. Here, $\overline{a} = (3/4\pi n_e)^{1/3}$ is the average distance between the electrons, which is also known as the Wigner-Seitz radius, and T_e and n_e are the electron temperature and density of the plasma, respectively.

For treating the warm and hot dense plasmas with a wide range of temperatures and densities, an atomic-state-dependent screening model [29] is proposed that can describe the interaction between charged particles, including the electron degeneracy effect. In this model, the plasma free electrons are assumed to be in equilibrium and described by the Fermi-Dirac distribution

$$f_{\mathrm{FD}}(p, r) = \frac{1}{1 + \exp\left[\frac{1}{T_e}\left(\frac{p^2}{2m_e} - \Phi(r) - \mu\right)\right]}, \tag{2}$$

where μ is the chemical potential of the plasma free electrons, $\Phi(r)$ is the total effective potential at position r, and p is the magnitude of electron momentum. However, in warm and hot dense plasma, the free electrons are transiently captured through the inelastic collision process such as three-body recombination, in which an electron transfers its energy and momentum to another free electron nearby and then recombines to the target ion with an unoccupied bound state. In the ASD model, the three-body recombination processes between the electron and the target ion have been taken into account in determining the electron distribution. For the convenience of numerical calculation, the recombined bound electrons are usually treated as negative-energy ones. For simplicity, the free electrons of the plasma are assumed to be in equilibrium and the steady-state approximation is applied to obtain the distribution of negative-energy state for the specific free-electron temperature and density. The atom with a specific bound state j can be formed through the three-body recombination of the target ion and its number density n^j_{atom} can be determined by a rate equation:

$$\frac{dn^j_{\mathrm{atom}}}{dt} = \sum_{i'}\left(n_e n^{j'}_{\mathrm{atom}} K_{j'j} - n_e n^j_{\mathrm{atom}} K_{jj'}\right) - n_e n^j_{\mathrm{atom}}\alpha_j + n_e^2 n_{\mathrm{ion}}\beta_j = 0. \tag{3}$$

Here, α_j, β_j, $K_{j'j}$, and $K_{jj'}$ are the rate coefficients of electron collision ionization, three-body recombination, excitation, and deexcitation, respectively.

Due to the degeneracy effect between the recombined and initially bound electrons, the negative-energy electron prefers to populate the unoccupied outer orbital and its momentum is larger than $\sqrt{2m_e[\varepsilon_b - \Phi(r)]}$. Therefore, the total plasma-electron density is given by

$$\rho(r) = \frac{1}{2\pi^2\hbar^3}\left[\int_{\sqrt{2m_e[\varepsilon_b - \Phi(r)]}}^{p_0} f_{\mathrm{FD}}(p, r)\chi(p, r)p^2 dp + \int_{p_0}^{\infty} f_{\mathrm{FD}}(p, r)p^2 dp\right]. \tag{4}$$

Here, $\chi(p, r)$ is the nonequilibrium coefficient obtained by solving Eq. (3), and ε_b is the energy of the outermost bound electron, which can significantly affect the negative-energy electron distribution of the target ion. On the right side of Eq. (4), the first term represents the distribution of negative-energy electron density.

Finally, the total effective potential of the target ion can be obtained from

$$\Phi(r) = \int \frac{1}{|r - r'|}[Z\delta(r') - \rho_b(r') - \delta\rho(r')]dr, \tag{5}$$

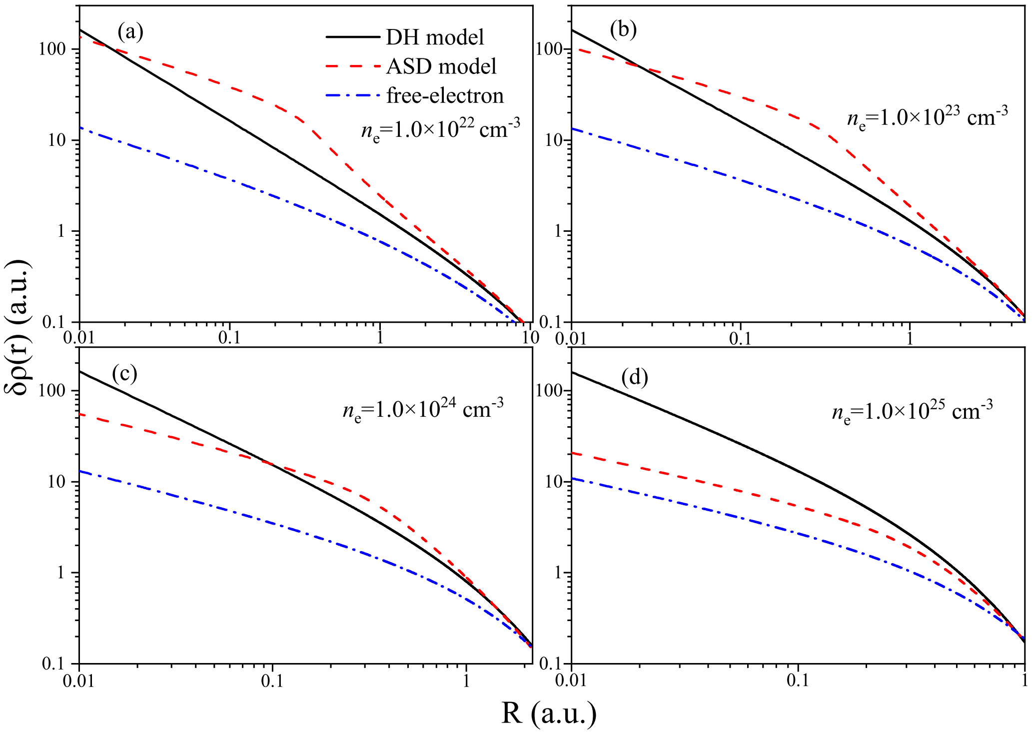

FIG. 1. Electron density fluctuations of the C^{5+} ion embedded in hot and dense plasmas from the screening model potential of the DH (solid lines), ASD (dashed lines), and free-electron (dash-dotted lines) models, respectively. The mean electron density n_e is (a) 1.0×10^{22}, (b) 1.0×10^{23}, (c) 1.0×10^{24}, and (d) 1.0×10^{25} cm^{-3}, respectively, and the temperature T_e is 100 eV. The distance R ranges from 0 to $\overline{a}$.

where $\delta\rho(r) = \rho(r) - \rho_e$ is the plasma-electron density fluctuation induced by the presence of the target ion, and $\Phi(r)$ and $\delta\rho(r)$ are dependent on each other and can be calculated with an iteration approach. The details of the derivation of the ASD model potential are presented in Ref. [29] and its supplementary material.

In warm and hot dense plasmas with high-density free electrons, three-body recombination processes will occur significantly as the free electrons approach the target ion, and then affect the electron distribution of the target ion. As shown in Eq. (4), the electron density distribution of the ASD model contains both free electrons and negative-energy electrons produced by the three-body recombination process between the plasma electrons and the target ion. However, in previous screening models, such as the uniform electron gas model [34] and self-consistent field ion sphere model [35,36], only elastic collision processes are considered, and free electrons with momentum $p > p_0 = \sqrt{2m_e\Phi(r)}$ are also applied to the Fermi-Dirac distribution to guarantee the positive electron energy. To illustrate the feature of the ASD screening model, Fig. 1 presents the plasma-electron density fluctuations $\delta\rho(r)$ of the C^{5+} ion embedded in warm and hot dense plasmas obtained from the present ASD model, as well as the DH and free-electron models. Due to the presence of negative-energy electrons, the density fluctuation of the ASD model in Fig. 1 is significantly larger than that of the free-electron model, in which only the contributions of elastic collision processes are considered and the plasma-electron density is obtained by $\rho(r) = 1/(2\pi^2\hbar^3)\int_{p_0}^{\infty} f_{\mathrm{FD}}(p,r)p^2dp$. As the density increases, the strong degeneracy effect causes the three-body recombination rate to decrease, indicating a decrease in negative-energy electron density. Therefore, the density fluctuation of the ASD model tends to that of the free-electron model. The density comparison between these two models above indicates that inelastic collision processes, especially three-body recombination, are important and cannot be ignored in warm and hot dense plasmas. As shown in Fig. 1, at low density, the ASD model exhibits larger density fluctuations than the DH model. It should be noted that when electrons are close to the nucleus, the electron density increases rapidly, and the induced electron degeneracy effect becomes important. This leads to a lower electron density fluctuation $\delta\rho(r)$ in the ASD model, while the DH model neglects this effect, resulting in an overestimation of $\delta\rho(r)$. As the distance R between electrons and the nucleus increases, the electron density fluctuations of the ASD model converge to those of the DH model. As electron density increases up to 1.0×10^{25} cm^{-3}, the plasma coupling and degeneracy effect enhance, therefore the electron density fluctuation of the DH model is larger than that of the ASD model.

These obvious differences in electron density fluctuations between the ASD model and the other two models are further reflected in the plasma screening effect and the wavefunction, which further affect the ionization energy and photoionization cross section of the embedded ions.

B. Relativistic energies and wavefunctions

After considering the plasma screening effect, the Dirac Hamiltonian for a hydrogenlike atom is given by

$$H = c\boldsymbol{\alpha}\cdot\mathbf{p} + (\beta - 1)c^2 + V(r), \tag{6}$$

where c is the speed of light, $\boldsymbol{\alpha}$ and β are Dirac matrices, and $\mathbf{p}$ is the momentum operator. The potential energy term $V(r)$ includes the nuclear potential and the external field generated by plasma screening. In the ASD model, this term is represented as

$$V(r) = -\frac{Z}{r} + \int \frac{\delta\rho(r')}{|r-r'|}dr. \tag{7}$$

In the DH model, $V(r)$ has the form of Eq. (1).

The Dirac state of a bound or continuum electron is expressed as

$$\psi_{g\kappa m}(Z,\lambda_D;r,\theta,\varphi) = \frac{1}{r}\begin{bmatrix} P_{g\kappa}(Z,\lambda_D;r)\chi_{\kappa m}(\theta,\varphi) \\ iQ_{g\kappa}(Z,\lambda_D;r)\chi_{-\kappa m}(\theta,\varphi)\end{bmatrix}, \tag{8}$$

where $P_{g,k}(Z;r)$ and $Q_{g,k}(Z;r)$ are the large and small components of the radial wavefunction, respectively. For bound states $g=n$, with n being the principal quantum number of the bound electron, and for continuum states $g=\varepsilon$, with $\varepsilon = (k^2c^2+c^4)^{1/2}-c^2$ being the kinetic energy of the continuum electron. $\chi_{km}(\theta,\varphi)$ in Eq. (8) is the spin angular function:

$$\chi_{km}(\theta,\varphi) = \sum_{\sigma=\pm 1/2}\left\langle lm-\sigma\frac{1}{2}\sigma\middle|l\frac{1}{2}jm\right\rangle Y_l^{m-\sigma}(\theta,\varphi)\phi^{\sigma}, \tag{9}$$

where $\langle lm{-}\sigma\frac{1}{2}\sigma|l\frac{1}{2}jm\rangle$ are the Clebsch-Gordan coefficients, $Y_l^{m-\sigma}(\theta,\varphi)$ are the spherical harmonics, and ϕ^σ are the spin basis function. The radial wavefunctions for both the bound and the continuum states of a hydrogenlike ion satisfy the coupled Dirac equations [37]

$$\begin{pmatrix} V(r)-E_{gk}(Z) & c\left(\frac{k}{r}-\frac{d}{dr}\right) \\ c\left(\frac{k}{r}+\frac{d}{dr}\right) & V(r)-2c^2-E_{gk}(Z)\end{pmatrix}\begin{pmatrix} P_{gk}(Z;r) \\ Q_{gk}(Z;r)\end{pmatrix} = 0, \tag{10}$$

with $E_{gk}<0$ for bound states and $E_{gk}>0$ for continuum states. Moreover, the radial wavefunctions of the bound and continuum states satisfy the orthogonality conditions

$$\begin{aligned}&\int_0^\infty d\rho[P_{nk}(Z;r)P_{n'k}(Z;r)+Q_{nk}(Z;r)Q_{n'k}(Z;r)] = \delta_{nn'},\\ &\int_0^\infty d\rho[P_{\varepsilon k}(Z;r)P_{\varepsilon' k}(Z;r)+Q_{\varepsilon k}(Z;r)Q_{\varepsilon' k}(Z;r)]\\ &\quad = \delta(\varepsilon-\varepsilon').\end{aligned} \tag{11}$$

The relativistic Wentzel-Kramers-Brillouin method [38] is used to normalize the continuum wavefunctions. The modified GRASP2K [37,39] and CONTWVSA [40] codes are used to obtain the relativistic bound and continuum wavefunctions.

C. Relativistic photoionization cross section

The relativistic photoionization cross section from the initial state a with total angular momentum j_a to a final continuum state b is given by

$$\sigma_{ab}^{\mathrm{PI}} = 2\pi^2\alpha\frac{df_{ab}}{d\varepsilon}, \tag{12}$$

where α is the fine-structure constant and $df_{ab}/d\varepsilon$ is the density of the oscillator strength:

$$\frac{df_{ab}}{d\varepsilon} = \frac{\pi c}{(2j_a+1)(2L+1)\omega^2}\left|\langle\psi_{nk}\|\widehat{\boldsymbol{O}}^{(L)}\|\psi_{\varepsilon k'}\rangle\right|^2. \tag{13}$$

Here ψ_{nk} and $\psi_{\varepsilon k'}$ are the initial- and final-state electron wavefunctions, respectively. $\widehat{\boldsymbol{O}}^{(L)}$ is the multipole radiation field operator of order L. The transition matrix element $\langle\psi_{nk}\|\widehat{\boldsymbol{O}}^{(L)}\|\psi_{\varepsilon k'}\rangle$ for the dipole transitions ($L=1$) has the form of

$$\begin{aligned}\langle\psi_{nk}\|\widehat{\boldsymbol{O}}^{(L)}\|\psi_{\varepsilon k'}\rangle &= \left(\frac{(2j_b+1)\omega}{\pi c}\right)^{1/2}(-1)^{j_a-1/2}\\ &\quad\times\begin{pmatrix} j_a & L & j_b \\ 1/2 & 0 & -1/2\end{pmatrix}\overline{M}_{ab}(\omega,G_L),\end{aligned} \tag{14}$$

where $\overline{M}_{ab}$ is the transition integral defined in Refs. [37,41].

In this work, the results of photoionization cross sections are calculated in the Coulomb gauge [41]. For the isolated C^{5+} ion, the photoionization cross sections are calculated by employing both Coulomb and Babushkin gauges, and it is found that the cross sections in these two gauges are in good agreement.

III. RESULTS AND DISCUSSION

In this work, we investigate the ground-state photoionization process of C^{5+} ions in warm and hot dense plasma environments with electron density and temperature ranges of $n_e = 1.0\times10^{22}-1.6\times10^{25}\ \mathrm{cm}^{-3}$ and $T_e = 20-280$ eV, respectively. Based on the methods discussed above, we obtain the wavefunctions and energy states of the isolated C^{5+} ion. Additionally, we calculate the wavefunctions and energy states for the C^{5+} ion embedded in plasmas, incorporating plasma screening effects through the ASD [29], DH [14,23], and free-electron models [29]. The present ionization energy of the ground state of an isolated C^{5+} ion is 18.0086 a.u., which agrees well with the National Institute of Standards and Technology [42] result of 18.0069 a.u.

To understand the behavior of the electron wavefunctions while considering the plasma screening effect, we calculate the large components of the continuum wavefunctions $\varepsilon p_{1/2}$ for the C^{5+} ion using the present ASD model with photoelectron energies of $\varepsilon = 0.5$ a.u. and $\varepsilon = 5$ a.u., respectively. For comparison, the results from the DH and free-electron models, as well as the isolated C^{5+} ion are also calculated, as shown in Figs. 2(a) and 2(b). The phase and amplitude of the continuum wavefunction are changed significantly due to the plasma screening effect. For the case of $\varepsilon = 0.5$ a.u., there are noticeable differences in the results between these three screening models, which is expected to further affect the energy levels and cross sections. For $\varepsilon = 5$ a.u., the continuum wavefunction from the ASD is close to that from the DH and free-electron models, and the isolated system, in comparison with the case of $\varepsilon = 0.5$ a.u. There are significant discrepancies in the amplitude and phase between the wavefunction of low- and high-energy electrons, and the amplitude decreases as the photoelectron energy increases. This indicates that plasma screening has a greater influence on the wavefunction of low-energy electrons than of high-energy electrons. The variation trend between different screening models of the continuum wavefunctions is consistent with the density fluctuations [Fig. 1(d)]. It can be seen that the density distribution of the DH model is the largest, resulting in the

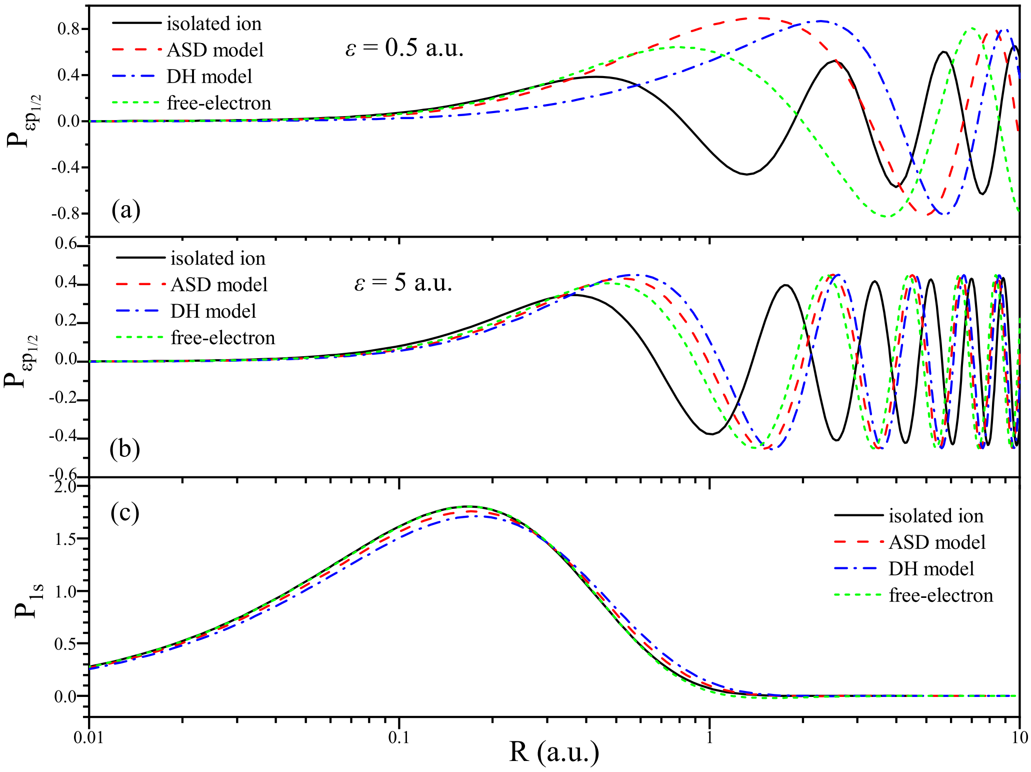

FIG. 2. Large components of continuum wavefunctions $\varepsilon p_{1/2}$ of the C^{5+} ion for the photoelectron energy (a) $\varepsilon = 0.5$ a.u. and (b) $\varepsilon = 5$ a.u. for isolated (solid lines), ASD (dashed lines), DH (dash-dotted lines), and free-electron (short-dashed lines) models, respectively. (c) Large components of bound wavefunctions $1s_{1/2}$ for different models. The plasma-electron temperature and density are $T_e = 100$ eV and $n_e = 1.0\times10^{25}$ cm^{-3}, respectively.

strongest screening effect and the weakest attraction effect on the electron, leading to an increase in the average distance between the electron and nucleus, as shown in the continuum wavefunctions in Figs. 2(a) and 2(b).

We also compare the large components of the bound wavefunction of the 1s radial orbital between these models, as shown in Fig. 2(c). It is found that the screening effect has a slight impact on the bound-state wavefunction. Considering its impact on both continuum and bound-state wavefunctions, the plasma screening effect will alter their overlap integral, according to Eq. (14), consequently affecting the ionization energy and photoionization cross section.

In a dense plasma, the strong screening significantly changes the photoionization cross sections near the ionization threshold, causing a redshift of the ionization energy [7]. These changes will have an impact on the radiation opacity [5,6]. In Fig. 3(a), we display the photoionization cross section obtained from the present ASD model together with the DH and free-electron screening models as functions of photon energy. These cross sections exhibit a rapid increase from zero to a maximum at the ionization threshold due to plasma screening. This behavior is distinct from that of an isolated ion, where the cross section monotonically decreases from a definite value at the threshold. The nature of this phenomenon is that the Coulomb potential of an isolated system is long range, while the screening potential in the plasma is short range, following the low-energy Wigner threshold law [15,43]. Moreover, the shape resonance peak appears in cross section, which manifests as a sudden increase in cross section at the ionization threshold, as for example shown in the results of the ASD model at $n_e = 1.0\times10^{24}$ cm^{-3} [green lines in Fig. 3(a)]. Shape resonance appears due to the centrifugal barrier in the effective potential of the continuum channel $\varepsilon l'$ when $l' > 0$ [9,12]. The continuum electron stays temporarily in the interior of the effective potential, leading to resonance structures in the photoionization cross sections, presenting as π radian changes in the phase of the continuum wavefunctions. With the energy approaching the critical value (the binding energy becomes zero), the peak of the shape resonance becomes sharper, corresponding to a larger peak value, as for example shown in the results of the free-electron model at $n_e = 1.0\times10^{23}$cm^{-3} [blue line in Fig. 3(a)]. More details of the shape resonance phenomenon will be discussed later.

When the target ion is embedded in a plasma, the free electrons weaken the interaction between the bound electron and the nucleus. As a result, the bound electron is easier ionize. The negative-energy electron density has a positive effect on the depression of the ground-state ionization energy of the C^{5+} ion, which cannot be neglected. We can see from Fig. 3(a) that the ionization energy depression of the ASD model is generally larger than that of the free-electron model. At lower electron densities, such as 1.0×10^{22}, 1.0×10^{23}, and 1.0×10^{24}cm^{-3}, the ionization energy of the ASD model shows more depression than that of the DH model. However, at the electron density of 1.0×10^{25}cm^{-3}, the ionization energy of the DH model decreases more than that of the ASD model. To highlight the depression of ionization energy, we compare

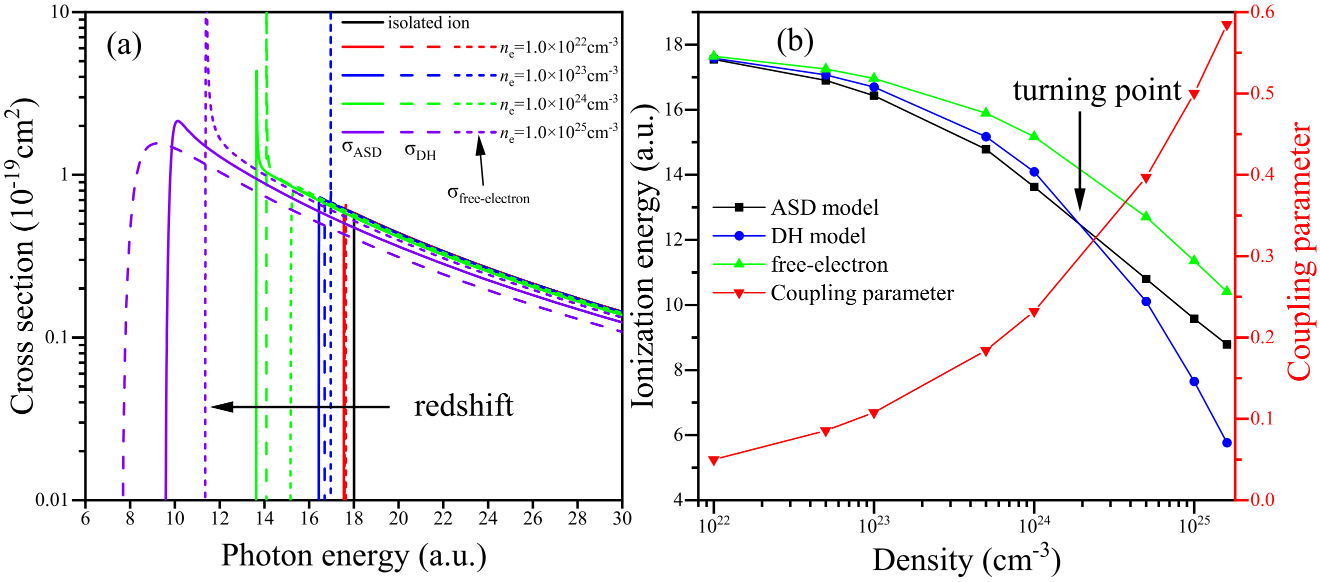

FIG. 3. (a) Density dependence of the $1s \rightarrow \varepsilon p_{1/2}$ photoionization cross section of C^{5+} ions from the ASD (solid lines), DH (dashed lines), and free-electron (short-dashed lines) models as a function of photon energy with electron temperature $T_e = 100$ eV and densities of 1.0×10^{22}, 1.0×10^{23}, 1.0×10^{24}, and $1.0\times10^{25}\text{cm}^{-3}$, respectively. (b) Ionization energy of the ground state of the C^{5+} ion as a function of electron density in plasmas with $T_e = 100$ eV and density ranges from $1.0\times10^{22}\text{cm}^{-3}$ to $1.6\times10^{25}\text{cm}^{-3}$. The ionization energy results from the ASD model are compared with those of the DH and free-electron models. The vertical axis on the right provides the Coulomb coupling parameter of the corresponding electron density.

the ionization energy of the ground state for the C^{5+} ion as a function of density among these models, as shown in Fig. 3(b). With increasing density, the screening effect enhances, resulting in a decrease in ionization energy.

At the low density, the ionization energy of the ASD model is consistent with that of the DH and free-electron models. As the density increases, the ionization energies of the ASD and DH models decrease rapidly comparing that of the free-electron model. However, the ionization energy of the DH model decreases much more than the ASD model, resulting in a turning point appearing between densities of 1.0×10^{24} and 5.0×10^{24} cm^{-3}. This density range corresponds to coupling parameters between 0.23 and 0.40 with $T_e = 100$ eV, indicating a moderately coupled plasma. This turning point is attributed to the fact that the ASD model takes account of the degeneracy effect through the distribution of negative-energy electrons, which decreases with increasing density, as we presented in Fig. 1. It is worth noting that at a density of $1.6\times10^{25}\text{cm}^{-3}$, the ionization energy of the ASD model decreases by 51% compared to the isolated system, and it is 52% greater than the DH model. At this density, the difference between these two models is at its maximum, as shown in Fig. 3(b). It can also be noticed that the ionization energy of the ASD model consistently remains lower than that of the free-electron model. As the density rises, the discrepancy of ionization energy between the ASD and free-electron model increases (reaching a maximum of 16% at $n_e = 1.0\times10^{25}\text{cm}^{-3}$) before decreasing. Meanwhile, the interaction distance between the free electrons and target ion decreases, leading to stronger coupling and more collisions between them. This results in a higher density of negative-energy electrons. With further increases in density, the electron degeneracy effect becomes stronger and the density of negative-energy electrons decreases. Eventually, the ASD model would converge to the free-electron model.

To analyze the plasma-electron density dependence of the photoionization cross section and the contribution of negative-energy electrons to the cross section, we provide the photoionization cross sections of the ASD, DH, and free-electron models in cases of different densities at $T_e = 100$ eV, as shown in Fig. 4(a). At specific electron temperatures, the plasma screening effect is enhanced with increasing density, and the photoionization cross sections of all three models significantly increase compared to the isolated ion. To evaluate the quantitative impact of plasma screening on cross sections, Fig. 4(b) displays the cross-section ratios of the screened models to the isolated ion. The results from the ASD model are larger than those obtained from the DH model, except at the electron density of $1.0\times10^{25}\text{cm}^{-3}$, where the cross-section ratios from the DH model are larger than those from the ASD model. This reversal phenomenon (also shown in Fig. 1) occurs due to the reversal of the electron density fluctuation between the ASD and DH models in strongly coupled plasma. At this density, due to the screening effect, the peak value of the cross sections from the ASD and DH models increase by a factor of 4 and 3.5, respectively. Since the ASD model contains the distribution of the negative-energy electrons, it has a larger influence on the cross section than the free-electron model.

The shape resonance characteristic of the cross section strongly depends on the effective potential of the target ion. For the states with angular momentum $l > 0$, the effective potential V_{eff} includes a screening potential well (e.g., the DH model) and a centrifugal barrier, denoted as

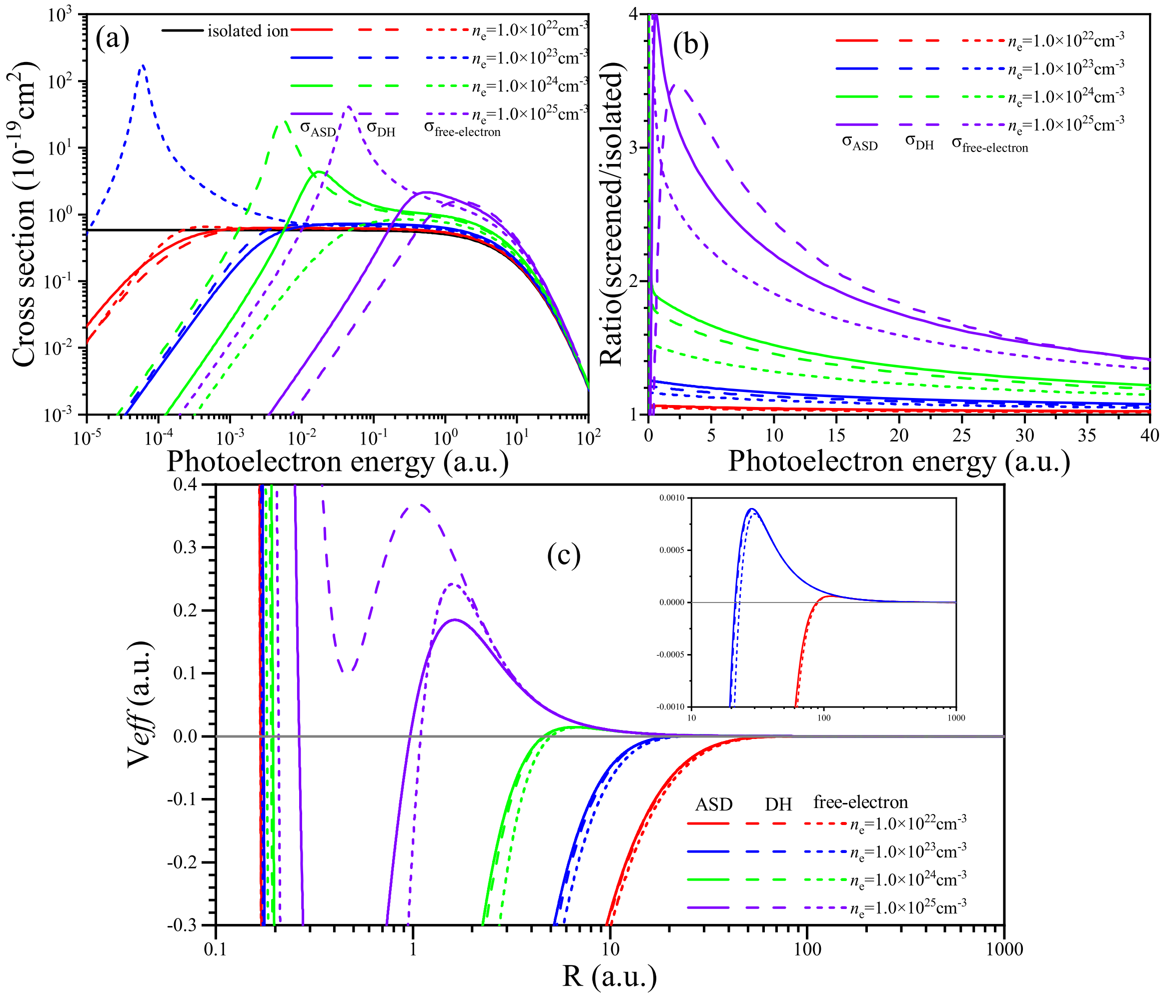

FIG. 4. (a) Photoionization cross sections for $1s \rightarrow \varepsilon p_{1/2}$ of the C^{5+} ion from the ASD (solid lines), DH (dashed lines), and free-electron (short-dashed lines) models as a function of photoelectron energy. (b) Cross-section ratios of these models to isolated results as a function of photoelectron energy. (c) Effective potential of the $1s \rightarrow \varepsilon p_{1/2}$ channel from the ASD, DH, and free-electron models. The small image in the upper right corner shows the part where the potential barrier appears at $n_e = 1.0\times10^{23}\text{cm}^{-3}$ and $n_e = 1.0\times10^{24}\text{cm}^{-3}$. The electron temperature $T_e = 100$ eV and densities are 1.0×10^{22}, 1.0×10^{23}, 1.0×10^{24}, and 1.0×10^{25}cm^{-3}, respectively.

$V_{\text{eff}}(r) = -Ze^{-r/\lambda_D}/r + l(l+1)/(2r^2)$. In Fig. 4(c), we present the effective potential of the C^{5+} ion of three models with different electron densities. Obviously, for any cross section with shape resonance, there exists a barrier of effective potential. Note that the existence of a barrier is necessary but not sufficient to assure the existence of shape resonance of the cross section. Therefore, we will further analyze the shape resonance phenomenon through the phase shift of a continuous electron in the following text. Moreover, the trend in cross-section variation with electron density corresponds to that of the effective potential barrier.

To explore the dependence of the photoionization cross section on electron temperature, we present the cross section in cases of different temperatures at $n_e = 1.0\times10^{24}\text{cm}^{-3}$, as shown in Fig. 5(a). It is found that the photoionization cross section for both the ASD and the DH models gradually increases as the electron temperature decreases, compared to the isolated system. For illustrating the quantitative impact of plasma screening on photoionization cross sections with varying plasma temperatures, the cross-section ratios of the screened to isolated ion are displayed in Fig. 5(b). The results from the ASD model exhibit larger values compared to those from the DH model, except at an electron temperature of 20 eV, where the cross section of the DH model is larger than that of the ASD. At this temperature, the coupling parameter is 1.16, indicating a strongly coupled plasma environment. The ASD model demonstrates lower density fluctuation than the DH model, which is attributed to its consideration of the degeneracy effect in such strongly coupled plasmas. This is evident in the apparent opposite variation observed in the cross section between these two models, similar to the trend depicted in Fig. 4.

In addition, due to the shape resonance, the photoionization cross section at different electron temperatures shows anomalous increases at the ionization threshold. Using $T_e = 20$ eV as an example, the cross section from the DH model shows a shape resonance peak while the ASD model does not, leading to a significant increase in the cross-section ratio of the DH

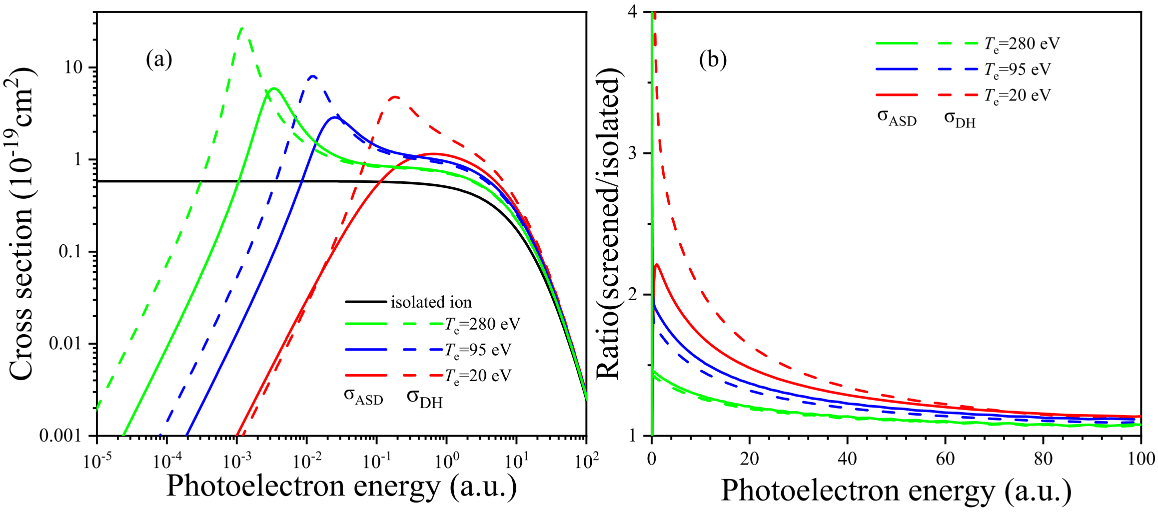

FIG. 5. (a) Photoionization cross sections for $1s \rightarrow \varepsilon p_{1/2}$ of the C^{5+} ion from the ASD (solid lines) and DH (dashed lines) models as a function of photoelectron energy. (b) Cross-section ratios of these models to isolated results. The electron density $n_e = 1.0\times10^{24}\text{cm}^{-3}$, and temperatures are 280, 95, and 20 eV, respectively.

model to the isolated system. At this temperature, the peak values of the cross section of the ASD and DH models are 2.2 and 8.4 times that of the isolated ion, respectively.

Similar to the DH model, the ASD model also exhibits shape resonance peaks in the photoionization cross section. However, the photoelectron energy positions related to these resonance peaks are different, as illustrated in Fig. 6(a). To explain this discrepancy, the phases of the continuum wavefunction with photoelectron energy $\varepsilon = 1.0\times10^{-4}$ a.u. (ASD model) and $\varepsilon = 1.0\times10^{-5}$ a.u. (DH model) are shown in

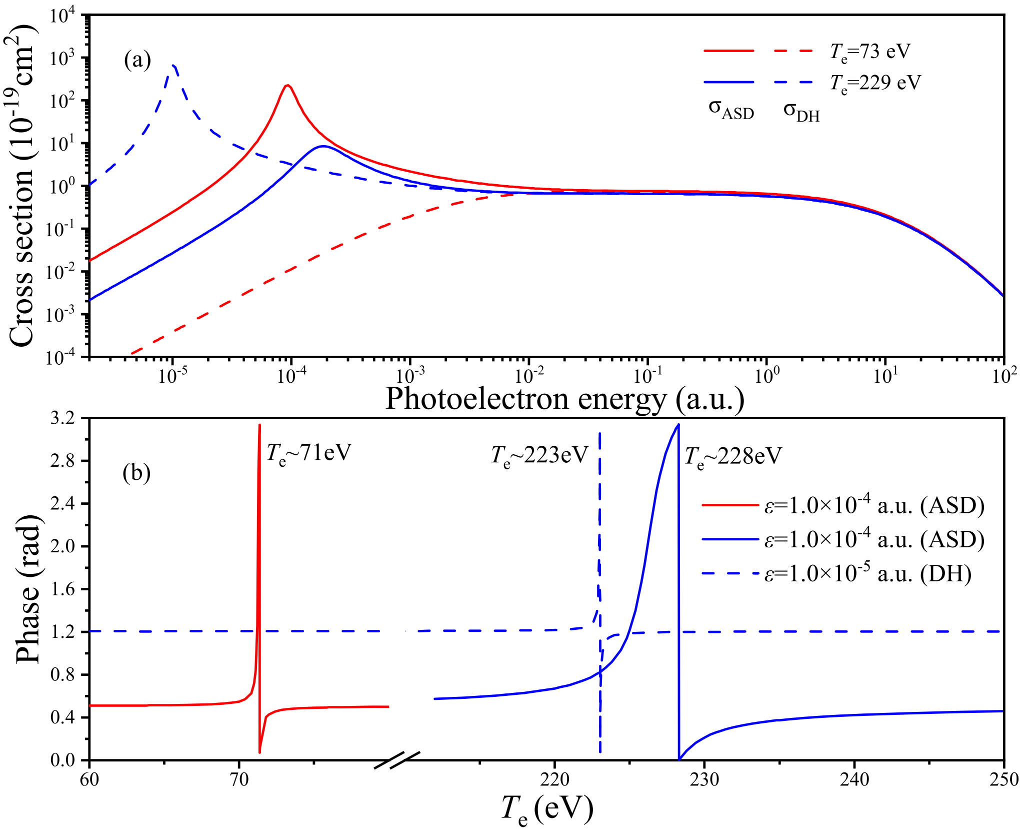

FIG. 6. (a) Photoionization cross section for $1s \rightarrow \varepsilon p_{1/2}$ of the C^{5+} ion from the ASD (solid lines) and DH (dashed lines) models as a function of photoelectron energy with electron density $n_e = 1.0\times10^{23}$ cm^{-3} and temperatures $T_e = 73$ eV and $T_e = 229$ eV. (b) Phases of the continuum wavefunction of $\varepsilon p_{1/2}$ for the C^{5+} ion as a function of electron temperature with $\varepsilon = 1.0\times10^{-4}$ a.u. (ASD model, solid lines) and $\varepsilon = 1.0\times10^{-5}$ a.u. (DH model, dashed line).

Fig. 6(b). At $T_e = 73$ eV, the cross section obtained by the ASD model exhibits a shape resonance peak at the photoelectron energy near 1.0×10^{-4} a.u., while the DH model does not. In this case, the photoelectron stays in the effective potential for a short time, leading to the resonance structure of the photoionization cross section near the ionization threshold and the sudden change of π radians in the phase, occurring near $T_e = 71$ eV as shown in Fig. 6(b). At $T_e = 229$ eV, the cross sections of both models exhibit shape resonance peaks at different photoelectron energies, which are near $\varepsilon = 1.0\times10^{-4}$ a.u. for the ASD model and $\varepsilon = 1.0\times10^{-5}$ a.u. for the DH model, respectively. The resonance peak is reflected by π radian changes in the phase of the continuum wavefunction at $T_e = 228$ eV with $\varepsilon = 1.0\times10^{-4}$ a.u. for the ASD model, and $T_e = 223$ eV with $\varepsilon = 1.0\times10^{-5}$ a.u. for the DH model, as depicted in Fig. 6(b). The ASD and DH models display different energy positions where the phase changes rapidly for the same transition channel in the same plasma environment. This difference results in a significant discrepancy in the position of the shape resonance peak. The effective plasma screening potential in this case could be inferred experimentally from the measured photoionization rate.

IV. CONCLUSION

We have employed the atomic-state-dependent screening model to investigate the photoionization processes of the hydrogenlike carbon ion embedded in warm and hot dense plasmas. Photoionization cross-section calculations in the dipole approximation have been carried out for the $1s \rightarrow \varepsilon p_{1/2}$ transition channel in various plasma environments, as well as the ionization energy of the ground state of the C^{5+} ion. The results show that the atomic photoionization results are sensitive to the plasma density and temperature. Due to the contribution of negative-energy electrons included in the ASD model, the obtained ionization energies and cross sections are significantly larger than those obtained from the free-electron model. The quantitative impact of plasma screening on the photoionization process is investigated employing the ASD model, and the difference in the results of ionization energy and cross section between the ASD and DH models are also analyzed. In weakly coupled plasmas, the ionization energies and cross sections from the ASD and DH models are very close to each other, while significant differences exist in moderately and strongly coupled plasmas. Additionally, the shape resonance phenomenon is observed in the cross section obtained from the ASD and DH models; however, the positions of their resonance peaks significantly differ, which may be utilized for identifying and distinguishing effective screening potentials in plasma. The proposed approach can be employed to investigate the plasma effects on the atomic structure and photoionization process of ions embedded in warm and hot dense plasmas, which may have promising implications for understanding the spectra observed in various astrophysical scenarios. With the advancement of experimental techniques, it is expected to achieve high-precision photoionization rate measurements in warm and hot dense plasma environments in the future. We hope that the present results will be validated in future studies of laboratory plasmas.

ACKNOWLEDGMENTS

This work was supported by the National Key Research and Development Program of China (Grant No. 2022YFA1602500) and the National Natural Science Foundation of China (Grants No. 12241410 and No. 12064041). We also acknowledge the National Key Laboratory of Computational Physics.

[1] B. A. Hammel, C. J. Keane, M. D. Cable, D. R. Kania, J. D. Kilkenny, R. W. Lee, and R. Pasha, X-ray spectroscopic measurements of high densities and temperatures from indirectly driven inertial confinement fusion capsules, Phys. Rev. Lett. **70**, 1263 (1993).

[2] M. D. Cable, S. P. Hatchett, J. A. Caird, J. D. Kilkenny, H. N. Kornblum, S. M. Lane, C. Laumann, R. A. Lerche, T. J. Murphy, J. Murray, M. B. Nelson, D. W. Phillion, H. Powell, and D. B. Ress, Indirectly driven, high convergence inertial confinement fusion implosions, Phys. Rev. Lett. **73**, 2316 (1994).

[3] J. L. Zeng, Y. J. Li, Y. Hou, C. Gao, and J. M. Yuan, Ionization potential depression and ionization balance in dense carbon plasma under solar and stellar interior conditions, Astron. Astrophys. **644**, A92 (2020).

[4] C. A. Iglesias and S. B. Hansen, Fe XVII opacity at solar interior conditions, Astrophys. J. **835**, 284 (2017).

[5] M. J. Seaton, Atomic data for opacity calculations: I. General description, J. Phys. B: At. Mol. Phys. **20**, 6363 (1987).

[6] D. G. Hummer, K. A. Berrington, W. Eissner, Anil K. Pradhan, H. E. Saraph, and J. A. Tully, Atomic data from the IRON project I. Goals and methods, Astron. Astrophys. **279**, 298 (1993).

[7] L. B. Zhao and Y. K. Ho, Influence of plasma environments on photoionization of atoms, Phys. Plasmas **11**, 4 (2004).

[8] S. Fritzsche, J. Nikkinen, S.-M. Huttula, H. Aksela, M. Huttula, and S. Aksela, Interferences in the $3p^4nl$ satellite emission following the excitation of argon across the $2p^5_{1/2}4s$ and $2p^5_{3/2}3d$ $J = 1$ resonances, Phys. Rev. A **75**, 012501 (2007).

[9] Y. Y. Qi, J. G. Wang, and R. K. Janev, Dynamics of photoionization of hydrogenlike ions in Debye plasmas, Phys. Rev. A **80**, 063404 (2009).

[10] L. Y. Xie, J. G. Wang, and R. K. Janev, Relativistic effects in the photoionization of hydrogen-like ions with screened Coulomb interaction, Phys. Plasmas **21**, 063304 (2014).

[11] G. P. Zhao, L. Y. Xie, L. Liu, J. G. Wang, and R. K. Janev, Photoionization of C^{5+} ion in warm dense plasmas, Phys. Plasmas **25**, 083302 (2018).

[12] X.-M. Tong, J.-M. Li, and R. H. Pratt, Delayed maxima in photoionization cross sections of atomic ions, Phys. Rev. A **42**, 5348 (1990).

[13] Y. Y. Qi, J. G. Wang, and R. K. Janev, Multiple series of shape resonances and near-zero-energy cross section enhancements in photoionization of hydrogen-like ions with screened Coulomb interaction, Eur. Phys. J. D **63**, 327 (2011).

[14] D. Salzman, *Atomic Physics in Hot Plasmas* (Oxford University Press, Oxford, 1998).

[15] S. Ichimaru, Strongly coupled plasmas: High-density classical plasmas and degenerate electron liquids, Rev. Mod. Phys. **54**, 1017 (1982).

[16] R. K. Janev, Z. Songbin, and W. Jianguo, Review of quantum collision dynamics in Debye plasmas, Matter Radiat. Extremes **1**, 237 (2016).

[17] S. Sahoo and Y. K. Ho, Photoionization of Li and Na in Debye plasma environments, Phys. Plasmas **13**, 063301 (2006).

[18] Y. Y. Qi, Y. Wu, and J. G. Wang, Photoionization of Li and radiative recombination of Li^{+} in Debye plasmas, Phys. Plasmas **16**, 033507 (2009).

[19] C. Y. Lin and Y. K. Ho, Quadrupole photoionization of hydrogen atoms in Debye plasmas, Phys. Plasmas **17**, 093302 (2010).

[20] T. N. Chang and T. K. Fang, Atomic photoionization in a changing plasma environment, Phys. Rev. A **88**, 023406 (2013).

[21] T. N. Chang, T. K. Fang, and Y. K. Ho, One- and two-photon ionization of hydrogen atom embedded in Debye plasmas, Phys. Plasmas **20**, 092110 (2013).

[22] Y.-D. Jung, Plasma screening effects on photoionizations in weakly coupled plasmas, Phys. Plasmas **5**, 3781 (1998).

[23] P. Debye and E. Hückel, The interionic attraction theory of deviations from ideal behavior in solution, Phys. Z. **24**, 185 (1923).

[24] M. Das, Effect of strongly coupled plasma on photoionization cross section, Phys. Plasmas **21**, 012709 (2014).

[25] Z.-B. Chen and K. Wang, Photoionization of h-like C^{5+} ion in the presence of a strongly coupled plasma environment, J. Quant. Spectrosc. Radiat. Transfer **245**, 106847 (2020).

[26] R. Sharma and A. Goyal, Strongly coupled plasma effect on excitation energies of O-like ions and photoionization of F-like ions, Indian J. Phys. **96**, 1829 (2022).

[27] Y. Y. Qi, J. G. Wang, and R. K. Janev, Photoionization of hydrogen-like ions in dense quantum plasmas, Phys. Plasmas **24**, 062110 (2017).

[28] Z.-B. Chen and K. Ma, Practical theoretical expressions for ions embedded in Debye and quantum plasmas, Phys. Plasmas **26**, 082115 (2019).

[29] F. Y. Zhou, Y. Z. Qu, J. W. Gao, Y. L. Ma, Y. Wu, and J. G. Wang, Atomic-state-dependent screening model for hot and warm dense plasmas, Commun. Phys. **4**, 148 (2021).

[30] C. S. Wu, F. Y. Zhou, J. Yan, X. Gao, Y. Wu, and J. G. Wang, Ionization potential depression model for warm/hot and dense plasma, arXiv:2305.09371.

[31] J. Lindl, Development of the indirect-drive approach to inertial confinement fusion and the target physics basis for ignition and gain, Phys. Plasmas **2**, 3933 (1995).

[32] R. S. Craxton *et al.*, Direct-drive inertial confinement fusion: A review, Phys. Plasmas **22**, 110501 (2015).

[33] M. S. Murillo and J. C. Weisheit, Dense plasmas, screened interactions, and atomic ionization, Phys. Rep. **302**, 1 (1998).

[34] H. Nguyen, M. Koenig, D. Benredjem, M. Caby, and G. Coulaud, Atomic structure and polarization line shift in dense and hot plasmas, Phys. Rev. A **33**, 1279 (1986).

[35] B. F. Rozsnyai, Relativistic Hartree-Fock-Slater calculations for arbitrary temperature and matter density, Phys. Rev. A **5**, 1137 (1972).

[36] X. D. Li, Z. Z. Xu, and F. B. Rosmej, Exchange energy shifts under dense plasma conditions, J. Phys. B: At. Mol. Opt. Phys. **39**, 3373 (2006).

[37] K. G. Dyall, I. P. Grant, C. T. Johnson, F. A. Parpia, and E. P. Plummer, GRASP: A general-purpose relativistic atomic structure program, Comput. Phys. Commun. **55**, 425 (1989).

[38] W. F. Perger, Z. Halabuka, and D. Trautmann, Continuum wavefunction solver for GRASP, Comput. Phys. Commun. **76**, 250 (1993).

[39] P. Jönsson, X. He, C. Froese Fischer, and I. P. Grant, The grasp2K relativistic atomic structure package, Comput. Phys. Commun. **177**, 597 (2007).

[40] M. G. Tews and W. F. Perger, Standalone relativistic continuum wavefunction solver, Comput. Phys. Commun. **141**, 205 (2001).

[41] I. P. Grant, Gauge invariance and relativistic radiative transitions, J. Phys. B: At. Mol. Phys. **7**, 1458 (1974).

[42] Atomic Spectra Database|NIST, https://www.nist.gov/pml/atomic-spectra-database.

[43] J. Berkowitz, *Photoabsorption, Photoionization, and Photoelectron Spectroscopy* (Academic Press, New York, 1979).